

Cumulative Consensus Score: Label-Free and Model-Agnostic Evaluation of Object Detectors in Deployment

Avinaash Manoharan^{1,2}, Xiangyu Yin³, Domenik Helms¹, and Chih-Hong Cheng^{2,3}

Abstract—Evaluating object detection models in deployment is challenging because ground-truth annotations are rarely available. We introduce the Cumulative Consensus Score (CCS), a label-free metric that enables continuous monitoring and comparison of detectors in real-world settings. CCS applies test-time data augmentation to each image, collects predicted bounding boxes across augmented views, and computes overlaps using Intersection over Union. Maximum overlaps are normalized and averaged across augmentation pairs, yielding a measure of spatial consistency that serves as a proxy for reliability without annotations. In controlled experiments on Open Images and KITTI, CCS achieved over 90% congruence with F1-score, Probabilistic Detection Quality, and Optimal Correction Cost. The method is model-agnostic, working across single-stage and two-stage detectors, and operates at the case level to highlight under-performing scenarios. Altogether, CCS provides a robust foundation for DevOps-style monitoring of object detectors.

I. INTRODUCTION

Deep learning has enabled major advances in computer vision, particularly in safety-critical domains such as autonomous driving. However, the reliability of perception modules, including object detection, remains a concern. Object detectors can make errors under distribution shifts and inherently suffer from epistemic uncertainty, stemming from incomplete training data and limited coverage of real-world conditions [1]–[3]. This uncertainty makes it difficult for engineers and end users to judge whether a newly trained object detector is more trustworthy than an existing, well-established one. Ground-truth annotations are typically required for model evaluation, yet such labels are rarely available at deployment time. This creates a fundamental gap between the controlled conditions in the lab and the operational domain, where continuous model monitoring and safe upgrades are most needed.

To address this challenge, we introduce the *Cumulative Consensus Score (CCS)*, a label-free method for evaluating object detectors in deployment. CCS builds on the idea of functional monitoring by enabling direct comparison of a new detector against an existing baseline without requiring annotated data. Its central principle is to assess the *spatial consistency of predictions*: if a detector is reliable, its outputs should remain stable when the input is subjected to benign transformations. By turning this stability into a measurable signal, CCS provides a practical proxy for reliability and offers a path toward scalable, deployment-time evaluation.

A key difficulty in designing CCS is that many uncertainty estimation techniques require architectural changes or large ensembles of models, which make fair comparisons costly and impractical. CCS avoids these drawbacks by using Test-Time Data Augmentation (TTDA) that preserves the detector architecture and requires no additional training. In practice, several photometric variations of an image are processed by the detector to produce bounding boxes. The overlap between bounding boxes from different augmentations is then quantified using Intersection over Union (IoU). For each bounding box, the best-matching box across augmentations is identified, and these maximum overlaps are averaged to produce a consensus score. By aggregating these scores across augmentation pairs, CCS provides a single value that reflects the stability of predictions at the image level, enabling the comparison of two object detectors. As the design is independent of model architecture, CCS can be applied uniformly across both single-stage and two-stage detectors, making it broadly suitable for real-world monitoring pipelines.

We validate CCS in controlled experiments by comparing its outputs against ground-truth-based metrics including F1 score, Probabilistic Detection Quality (pPDQ), and Optimal Correction Cost (OC-cost). Experiments across datasets such as Open Images [4] and KITTI [5], and across architectures including Faster R-CNN [6], RetinaNet [7] and SSD [8] show that CCS achieves over 90% congruence with these established measures. Importantly, CCS provides results at the image level rather than only at the dataset level. This enables the identification of under-performing cases where a detector produces unstable or inconsistent predictions across augmentations, allowing engineers to pinpoint problematic inputs and guide targeted improvements. These results demonstrate that CCS provides a robust and scalable foundation for DevOps-style monitoring of object detectors without reliance on costly human annotation.

II. RELATED WORK

A central challenge in deploying object detectors is the lack of ground-truth annotations in the operational domain, which makes supervised reliability metrics (e.g., mAP or F1-score) impractical. To address this, several works have explored label-free indicators of reliability. Schmidt et al. [9] introduced a consensus score within an ensemble-driven active learning framework, but their reliance on Bayesian model variants [10], [11] and ensembles makes deployment costly. Yang et al. [12] proposed the Box Stability Score (BoS), which correlates stability under feature dropout with

¹ DLR Institute of Systems Engineering for Future Mobility, Germany

² Carl von Ossietzky University of Oldenburg, Germany

³ Chalmers University of Technology, Sweden

Contact: avinaash.manoharan@dlr.de, chih-hong.cheng@uol.de

downstream mAP, though it requires internal feature access. Yu et al. [13] designed the Detection Adaptation Score (DAS), combining prediction flatness and feature transferability for unsupervised checkpoint selection, but again depends on feature access and targets training-time model choice. Yu et al. [14] further extended consistency ideas to active learning by proposing CALD, reducing annotation effort but still relying on labeled data for retraining. The CCS method proposed in this paper complements these directions by retaining the idea of consistency as a reliability proxy while removing the need for ensembles, feature access, or annotation. By operating directly on detector outputs under TTDA, CCS is both model-agnostic and deployable, and uniquely enables per-image comparison between two detectors in the field. Conceptually, this use of test-time augmentation is related to randomized smoothing [15]–[17], which also aggregates predictions over perturbed inputs, though CCS focuses on lightweight functional monitoring rather than certified robustness.

In parallel, the field of *Probabilistic Object Detection* has aimed to provide explicit uncertainty estimates for classification and bounding box regression [18]–[21]. Such methods extend deterministic detectors to quantify epistemic uncertainty, often through architectural modifications or ensembles, thereby producing uncertainty-aware confidence scores. While these estimates are valuable, they remain expensive to obtain and are tied to specific detector designs. Moreover, commonly used evaluation metrics such as pPDQ [2] and OC-cost [22] require ground-truth annotations and have known limitations in scoring reliability [3], [23]. CCS complements this line of research by exploiting variability across test-time augmentations as a lightweight proxy for spatial uncertainty, aligning well with supervised metrics when ground truth is available, while remaining practical for deployment where labels are absent.

III. INSIDE CUMULATIVE CONSENSUS SCORE

This section describes the methodology for computing the Cumulative Consensus Score (CCS) at the image level. Fig. 1 illustrates the workflow and the mindset for how CCS is designed, as well as comparing the result of two object detectors f_1 and f_2 . Given an image img , TTDA is conducted to build M variations via techniques such as adding Gaussian noise or photometric augmentations such as shifting weather conditions. As there is no shearing or cropping of images in our augmentation pipeline, for all augmented images, any object (e.g., pedestrian) should be located at the same location in the image plane. In this regard, a *necessary condition* of a high-performing object detector is to generate bounding boxes among images that induce a larger overlap. In Fig. 1, object detector f_1 performs better, as the bounding boxes being produced across different images have higher overlap. As shown in subsequent paragraphs, CCS utilizes such a concept and characterizes the degree of overlap by computing an aggregated value utilizing the standard IoU computation across augmented images. Notably, the computation of CCS characterizes the subtlety that can

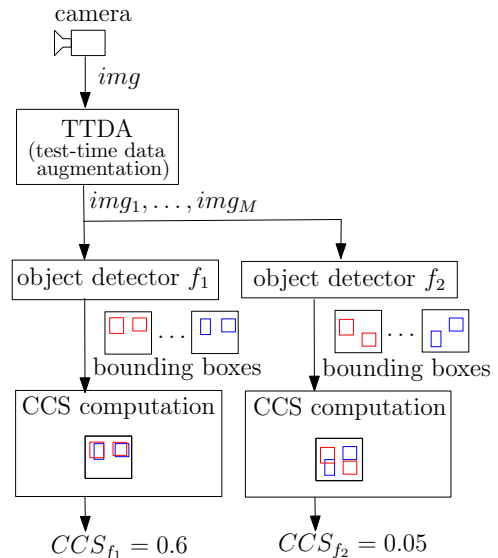


Fig. 1: Workflow of computing CCS and comparing the result of two object detectors f_1 , f_2 using the corresponding CCS values $\bar{\gamma}_{f_1}$, $\bar{\gamma}_{f_2}$.

occur when multiple objects are present in an image, so an extra association step is needed.

1) *Basic setting*: Let M denote the number of augmentations applied to each input image. For a given image, let N_i and N_j denote the number of bounding boxes predicted by the detector on the i^{th} and j^{th} augmentations, respectively. The Intersection over Union (IoU) matrix Ω_{ij} is then computed by comparing each predicted bounding box from the i^{th} augmentation with those from the j^{th} augmentation. Formally, the IoU matrix is defined as

$$\Omega_{ij} \in \mathbb{R}^{N_i \times N_j}, \quad i, j \in [1, M],$$

where each entry of Ω_{ij} represents the IoU between a bounding box from augmentation i and a bounding box from augmentation j . Since $N_i \neq N_j$ in general, Ω_{ij} is not necessarily a square matrix.

As an example, consider object detections from three image augmentations as shown in top left of Fig. 2, where bounding boxes in red, blue, and black are from augmentations indexed 1 to 3, respectively, and for all boxes of the same color, without loss of generality, assume that it is ordered from left to right¹. The resulting computation is shown at the bottom left of Fig. 2. For instance, the IoU matrix Ω_{12} has a value of

$$\Omega_{12} = \begin{pmatrix} 0.5625 & 0 \\ 0 & 0.5 \end{pmatrix},$$

where the top-left value of Ω_{12} reflects that the left two bounding boxes between red and blue have an IoU of 0.5625,

¹The computation of γ_{ij} , as detailed in Eq. (3), is invariant to any permutation of box order within either augmentation: taking a row-wise maximum removes column ordering, and summing over rows removes row ordering. This is the reason why our example of ordering boxes from left to right does not lose generality.

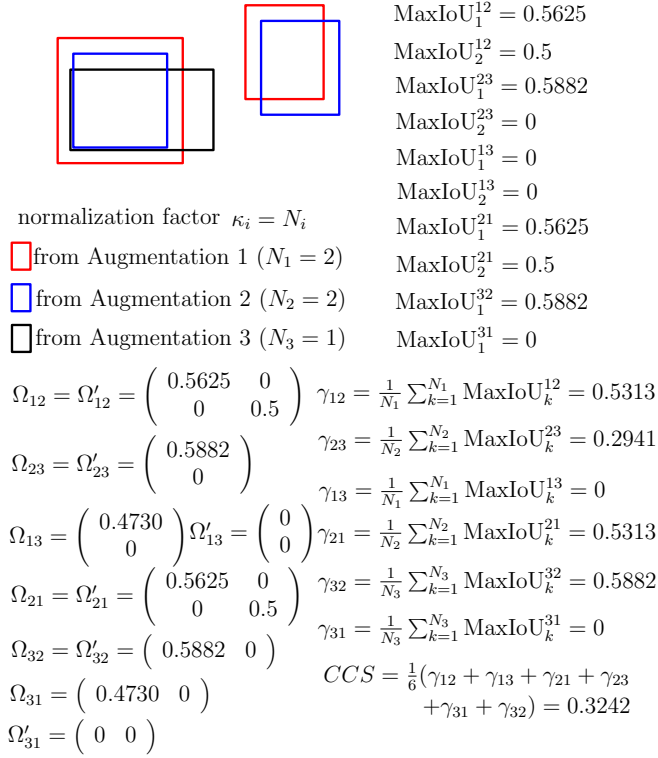


Fig. 2: Predictions from three augmentations and the associated CCS computation, including all intermediate steps, where bounding boxes of the same color are ordered from left to right.

and the top right value of Ω_{12} reflects that the left red bounding box has zero overlap with the right blue bounding box. Note that $\Omega_{23} = \begin{pmatrix} 0.5882 & 0 \\ 0 & 0 \end{pmatrix}^T$ is a 2×1 matrix, as there are two detected objects (in blue) in the 2nd augmented image and only one detected object (in black) in the 3rd augmented image.

2) *Apply thresholding to the IoU matrix:* Given an original IoU matrix Ω_{ij} , where element $\Omega_{ij}(k, l)$ denotes the Intersection over Union (IoU) between the k^{th} predicted bounding box from i -th augmentation and the l^{th} predicted bounding box from the j -th augmentation, we apply a threshold β to obtain a filtered IoU matrix Ω'_{ij} :

$$\Omega'_{ij}(k, l) \stackrel{\text{def}}{=} \begin{cases} \Omega_{ij}(k, l), & \text{if } \Omega_{ij}(k, l) \geq \beta \\ 0, & \text{otherwise} \end{cases} \quad (1)$$

Once the threshold β is applied, we transform Ω_{ij} to a new matrix Ω'_{ij} , where only significant IoU values (those exceeding the threshold) are retained, and all others are suppressed to 0. This step emphasizes meaningful overlaps and discards minor ones. The choice of β follows the convention established in [24], where an IoU of at least 0.5 is considered the minimum requirement for associating a detection with a ground-truth object. For the example in Fig. 2, as $\Omega_{13} = \begin{pmatrix} 0.4730 & 0 \\ 0 & 0 \end{pmatrix}^T$ has an element with a value 0.4730 being smaller than $\beta = 0.5$, in Ω'_{13} the value is suppressed to 0.

3) *Compute the maximum IoU value for each row in the filtered matrix:* For each row k in the filtered IoU matrix Ω'_{ij} , we compute the maximum IoU value that exceeds the threshold. This operation identifies the most significant overlap for each predicted bounding box from the i -th augmentation, relative to all predicted bounding boxes from the j -th augmentation:

$$\text{MaxIoU}_k^{ij} \stackrel{\text{def}}{=} \max\{\Omega'_{ij}(k, *)\}, \quad (2)$$

where $\Omega'_{ij}(k, *)$ denotes the set of all IoU values in row k of the filtered IoU matrix Ω' . Going back to the example in Fig. 2, $\text{MaxIoU}_1^{12} = \max(\Omega'_{12}(1, *)) = \max\{\Omega'_{12}(1, 1), \Omega'_{12}(1, 2)\} = 0.5625$.

4) *Calculate the pair-wise consensus score γ_{ij} :* The consensus score γ_{ij} is computed by summing the maximum IoU values obtained for each row of the filtered matrix.

$$\gamma_{ij} \stackrel{\text{def}}{=} \frac{1}{\kappa_i} \sum_{k=1}^{N_i} \text{MaxIoU}_k^{ij} \quad (3)$$

Eq. 3 succinctly represents the process of quantifying localization agreement across the i^{th} and j^{th} augmentations by considering only the most significant overlaps. The normalization by κ_i ensures that γ_{ij} is scaled relative to the number of detections, providing a consistent and unified measure of localization uncertainty across images with varying object counts. There are a few options in designing κ_i :

- 1) The simplest way is to set κ_i to be always constant across all augmentations, which in effect leads to no normalization. Apart from setting κ_i as 1, in our evaluation, we use the number of detected objects with a lower confidence threshold in the original image as κ_i (thereby being the same for all augmentations); such a number is normally larger than the number of bounding boxes, thereby leading to the resulting γ_{ij} to be less than 1. However, one can not guarantee that using N_0 leads to the resulting γ_{ij} being smaller than 1, as it is possible that an object detector, in the original un-augmented image, detects fewer objects.
- 2) Alternatively, one can let κ_i be N_i (i.e., to be augmentation dependent), thereby taking the value of γ_{ij} being always within the interval $[0, 1]$. Fig. 2 shows the computation where the value of κ_i equals N_i (i.e., $\kappa_1 = \kappa_2 = 2$ and $\kappa_3 = 1$). Nevertheless, the symmetry will be broken, i.e., $\gamma_{ij} \neq \gamma_{ji}$. As illustrated in Fig. 2, $\gamma_{23} \neq \gamma_{32}$ due to the number of detected objects in augmented images 2 and 3 being different.

Finally, we need to explicitly consider the case when N_i equals 0 (i.e., no objects are detected in the i -th augmentation), where we set the corresponding γ_{i*} or γ_{*i} to be 0.

5) *Calculate CCS via aggregation:* After computing the pairwise consensus score γ_{ij} for each valid augmentation pair, we obtain the Cumulative Consensus Score (CCS) via averaging the consensus scores across all unique augmentation pairs where $i \neq j$.

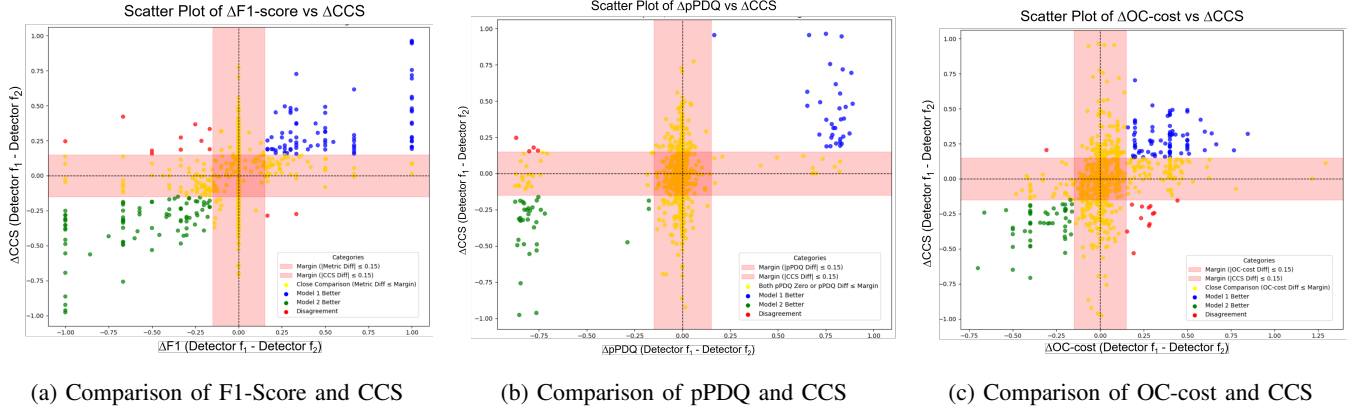


Fig. 3: Scatter plots comparing CCS with established metrics: F1-Score, pPDQ, and OC-cost.

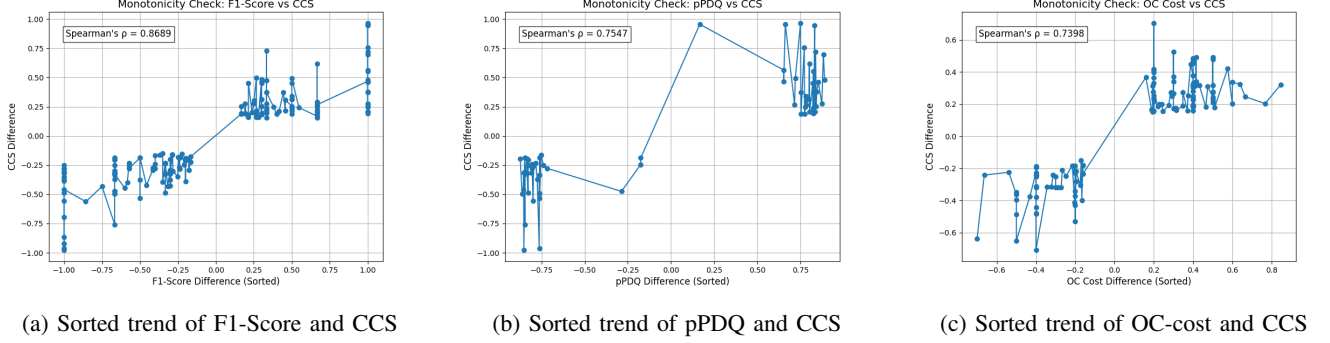


Fig. 4: Sorted trend analysis showing the alignment of CCS with F1-Score, pPDQ, and OC-cost.

$$CCS \stackrel{\text{def}}{=} \frac{1}{(M)(M-1)} \sum_{i=1}^M \sum_{\substack{j=1 \\ j \neq i}}^M \gamma_{ij} \quad (4)$$

By averaging across all pairwise comparisons with each γ_{ij} reflecting the imprecision of j -th prediction from the view of the i -th prediction, CCS provides a comprehensive uncertainty measure of localization consistency for the image, independent of the number of augmentations applied and independent of the underlying object detector architecture.

IV. EXPERIMENTS AND RESULTS

A. Experimental Setup

1) *Dataset*: We train object detectors on Open Images Dataset (OID) [4], [25] and evaluate on KITTI [5], [26]. Unless noted, KITTI is used for evaluation only.

2) *Evaluation metrics*: We compare CCS against F1-score, OC-cost, and pPDQ with definitions as follows:

- **F1-score**: Following [3], we use one-to-one matching at IoU threshold α_{iou} (specified with results). A prediction is a true positive (TP) iff its class matches the ground truth and $\text{IoU} \geq \alpha_{\text{iou}}$; otherwise it is a false positive (FP). Any unmatched ground-truth box is a false negative (FN). The F1-Score is then computed as:

$$\text{F1-Score} = 2 \frac{\text{Precision} \cdot \text{Recall}}{\text{Precision} + \text{Recall}}. \quad (5)$$

- **OC-cost**: OC-cost [22] evaluates detectors via minimum-cost bipartite matching between predictions and ground truths. Unmatched predictions or ground truths incur a constant penalty β_{dummy} , which Otani *et al.* [22] found to yield the best alignment with human preference at $\beta_{\text{dummy}} = 0.6$. The per-pair matching cost equals

$$C_{\text{total}} = \lambda C_{\text{loc}} + (1 - \lambda) C_{\text{cls}}, \quad (6)$$

where $C_{\text{loc}} = 1 - \text{IoU}$ denotes the localization cost and C_{cls} the classification cost. In our setup, we set $\lambda = 1$ to focus exclusively on localization.

- **pPDQ**: pPDQ [2] combines spatial and semantic uncertainty via the geometric mean between a ground truth $\mathcal{G}_i^{\text{img}}$ and a detection $\mathcal{D}_j^{\text{img}}$:

$$\text{pPDQ}(\mathcal{G}_i^{\text{img}}, \mathcal{D}_j^{\text{img}}) = \sqrt{Q_S(\mathcal{G}_i^{\text{img}}, \mathcal{D}_j^{\text{img}}) \cdot Q_L(\mathcal{G}_i^{\text{img}}, \mathcal{D}_j^{\text{img}})}. \quad (7)$$

Here Q_S measures how well the spatial probability distribution of a detection aligns with the ground truth, while Q_L is the probability the detector assigns to the correct class label. Unlike a simple L_2 norm, Q_S is formally defined as

$$Q_S(\mathcal{G}_i^{\text{img}}, \mathcal{D}_j^{\text{img}}) = \exp\left(-[L_{\text{FG}}(\mathcal{G}_i^{\text{img}}, \mathcal{D}_j^{\text{img}}) + L_{\text{BG}}(\mathcal{G}_i^{\text{img}}, \mathcal{D}_j^{\text{img}})]\right). \quad (8)$$

TABLE I: Comparison of old and new object detectors, both trained on 2000 Car and 2000 Truck samples from OID [25].

Metric	Old Model: Faster R-CNN ResNet-50 FPN (50 epochs)	New Model: RetinaNet ResNet-50 FPN (100 epochs)
Baseline COCO mAP	0.384	0.409
mAP (after training)	0.4307	0.4979
Validation Loss	0.1872	0.1746

where L_{FG} is the average negative log-probability that the detector assigns to pixels belonging to the ground-truth segment (foreground loss), and L_{BG} penalizes probability mass that the detector incorrectly assigns to pixels outside the ground-truth bounding box (background loss). *Implementation note.* Although PDQ was originally defined for pixel-accurate masks, following the work by Hall *et al.* [2] we adapt it to bounding boxes by assigning a foreground probability of $1 - \epsilon$ inside the predicted box and ϵ outside. We set $\epsilon = 0.1$ to enforce strict localization penalties suited for autonomous-driving scenarios and to avoid over-rewarding imprecise boxes.

B. Congruence of CCS with Established Metrics

This subsection evaluates how well CCS aligns with standard supervised metrics (Sec. IV-A.2). In Fig. 1, each image is processed by two object detectors f_1 and f_2 (Tab. I). For each metric $M \in \{F1, pPDQ, OC\text{-}Cost\}$ we obtain per-image scores M_{f_1} and M_{f_2} and form the deltas

$$\Delta M = M_{f_1} - M_{f_2}. \quad (9)$$

Similarly, the difference of CCS between the two models is computed as:

$$\Delta CCS = CCS_{f_1} - CCS_{f_2} \quad (10)$$

Fig. 3 plots ΔCCS against ΔM for model pairs in Tab. I. Agreement is quantified by (i) the congruence rate, the fraction of images where $\text{sign}(\Delta M) = \text{sign}(\Delta CCS)$ outside an indifference band $|\Delta| \leq \tau$ (we use $\tau = 0.15$ unless noted), and (ii) Spearman's ρ . Training and evaluation data follow Sec. IV-A.1; detailed statistics appear in Tab. II.

C. Observations from Fig. 3

In Fig. 3, each point is a test image; colors encode the level of agreement between CCS and other standard metrics.

- **Blue Dots:** $\Delta M > 0$ and $\Delta CCS > 0$ indicate that f_1 outperforms f_2 .
- **Green Dots:** $\Delta M < 0$ and $\Delta CCS < 0$ indicate that f_2 outperforms f_1 .
- **Red Dots:** CCS and the standard metric disagree on which model performs better.
- **Yellow Dots:** Differences that fall within predefined margins, indicating negligible variation:

TABLE II: Comparison of CCS and standard metrics (models and dataset in Tab. I)

Metric	Total Test Images	Yellow Dots	Images Consi- dered	Green Dots	Blue Dots	Red Dots	Congru- ence(%)
$\Delta F1$ vs ΔCCS	1000	822	178	86	80	12	93.26
$\Delta pPDQ$ vs ΔCCS	1000	929	71	34	33	4	94.37
ΔOC vs ΔCCS	1000	851	149	87	49	13	91.28

- Vertical margin ($|\Delta M| \leq 0.15$): negligible change under the standard metric.
- Horizontal margin ($|\Delta CCS| \leq 0.15$): negligible change under CCS, making ranking unreliable in operational domains without ground truths.

Alignment of blue and green points along the diagonal ($y = x$) in Fig. 3 indicates strong agreement between CCS and standard metrics. Conversely, numerous red points would indicate systematic discrepancies. However, we observe few red points and a high congruence rate. Yellow dots, representing instances of near-equivalent model performance, are excluded to emphasize nontrivial performance differences.

We next formalize the indifference margin τ , and demonstrate how it is chosen, fixed for reporting, and used to handle near-equivalent model performance.

a) *Margin τ :* Larger τ absorbs more points into yellow; smaller τ exposes more red (and blue/green) points. Our goal is to highlight *substantive* incongruence between ΔM and ΔCCS , not near-ties caused by small numerical or thresholding effects. When τ is too small (e.g., < 0.10), many “red” points arise from tiny, hard-to-interpret differences; for example, $\Delta CCS = -0.13$ vs. $\Delta M = +0.14$ flip signs while both magnitudes are modest, often due to localization jitter, IoU/NMS edge effects, or score calibration noise.

Before analyzing results, we adopted the following rule for setting τ : *choose the smallest τ within a plausible range $[0.10, 0.20]$ such that the remaining red points are predominantly attributable to interpretable causes* (e.g., missing/partial ground truth or small-magnitude metric-consensus mismatches). Applying this rule yields $\tau=0.15$ in our data. At this setting, most red points fall into two categories: (i) **Missing or incomplete ground truth**, which makes ΔM unreliable and induces apparent disagreements with ΔCCS ; (ii) **Small-magnitude metric-consensus mismatches**, where CCS assigns near-identical consensus while the standard metric flips sign due to thresholding/tie-breaking.

b) *Default and tuning:* We treat τ as a user-tunable tolerance. For all reported results, we fix a single default $\tau=0.15$, selected *a priori* using the rule as stated above, and do not tune it per dataset. Practitioners may increase τ to downweight near-ties or decrease it to surface finer disagreements, depending on application tolerance.

c) *Handling Near-Equivalent Model Performance:* In the chosen example, the presence of a large number of yellow dots can be attributed to the fact that both models

TABLE III: Comparison of CCS and F1-Score, pPDQ, and OC Cost across different architectures and training epochs

Training Dataset	Model Name	ΔM vs. ΔCCS	Congruence (%)	Spearman's ρ
Model Old: Images/class: 6000 Labels: Car, Truck Model New: Images/class: 6000 Labels: Car, Truck	Model Old: Faster R-CNN ResNet-101, 2 epochs (mAP: 0.3308, Val loss: 0.1940) Model New: SSD300 VGG16, 250 epochs (mAP: 0.5053, Val loss: 0.2092)	$\Delta F1$ vs. ΔCCS	97.97	0.8077
		$\Delta pPDQ$ vs. ΔCCS	96.51	0.7421
		ΔOC Cost vs. ΔCCS	91.73	0.6619
Model Old: Images/class: 2000 Labels: Car, Truck Model New: Images/class: 6000 Labels: Car, Truck	Model Old: RetinaNet ResNet-50 FPN, 50 epochs (mAP: 0.4837, Val loss: 0.1676) Model New: RetinaNet ResNet-50 FPN, 150 epochs (mAP: 0.5194, Val loss: 0.1619)	$\Delta F1$ vs. ΔCCS	94.51	0.8696
		$\Delta pPDQ$ vs. ΔCCS	90.16	0.7354
		ΔOC Cost vs. ΔCCS	87.70	0.7158

 TABLE IV: Robustness of CCS congruence across different augmentation seeds. Reported values are Spearman's ρ between ΔCCS and standard metrics ΔM for the detector setup described in Tab. I.

Aug. Seed	$\rho(\Delta F1, \Delta CCS)$	$\rho(\Delta pPDQ, \Delta CCS)$	$\rho(\Delta OC\text{-cost}, \Delta CCS)$
15	0.8529	0.7510	0.7647
33	0.8508	0.7514	0.7515
55	0.8541	0.7377	0.7506
101	0.8544	0.7539	0.8049
150	0.8509	0.7503	0.7620

exhibit nearly identical mAP scores. This specific corner case was chosen to demonstrate CCS's effectiveness even with similar-performing models. Such a capability is crucial in real-world applications, as it enables smooth model updates and controlled transitions from old to new models.

D. Sorted Trend Analysis for Congruence Assessment

To assess how well CCS aligns with standard metrics, we perform sorted trend analysis by first filtering out red and yellow dots, and retaining only green and blue ones. Images are then sorted by their ΔM values, and corresponding ΔCCS values are examined for monotonic trends. As shown in Fig. 4, the relationship between ΔM and ΔCCS is generally monotonic, motivating the use of Spearman's rank correlation coefficient (ρ), which quantifies monotonic relationships without assuming linearity. It is defined as $\rho = 1 - \frac{6 \sum d_i^2}{n(n^2 - 1)}$, where d_i is the difference between the ranks of ΔM and ΔCCS for the i -th image, and n is the total number of images considered. A higher ρ implies stronger agreement between CCS and the standard metric.

E. Observations from Tab. II

Tab. II shows that the percentage of congruence (i.e., Congruence (%) = $\frac{\text{Green} + \text{Blue}}{\text{Considered}} \times 100$) is consistently high across all metrics, with F1-score (93.26%), pPDQ (94.37%), and OC Cost (91.28%), indicating strong agreement between CCS and standard evaluation metrics. The Spearman's rank correlation coefficient (ρ) values for all comparisons also

remain high, confirming a monotonic relationship between ΔM and ΔCCS .

TABLE V: CCS post-processing time per image on CPU (single-process Python; NumPy/SciPy).

Device	CPU (NumPy/SciPy)
Host CPU	2×EPYC 7742; SMT on; 256 threads; 8 NUMA nodes
M (aug/image)	9
Boxes/aug (N_i) <i>KITTI</i> (two classes: cars, trucks)	≤ 5
Per-pair time [ms]	0.03–0.16
Per-image time [ms]	2.9–11.4
Timed steps	build Ω_{ij} ; threshold $\rightarrow \Omega'_{ij}$ (1); row-wise max MaxIoU_k^{ij} ; $\text{sum}/\kappa_i \rightarrow \gamma_{ij}$ (3)
Final average to CCS (Eq. 4)	No (< 0.1 ms)

F. Robustness to Augmentation Seeds and Model Architectures

Since CCS uses TTDA, we verified that results are not tied to a specific random seed. Tab. IV shows five representative seeds for clarity, while the full study (15 seeds) was conducted using the detector setup in Tab. I. Across all seeds, the Spearman's ρ values remain tightly clustered: $\rho(\Delta F1, \Delta CCS) = 0.8531 \pm 0.0016$ (mean \pm std, 95% CI: ± 0.0009), $\rho(\Delta pPDQ, \Delta CCS) = 0.7461 \pm 0.0076$ (95% CI: ± 0.0041), and $\rho(\Delta OC\text{-cost}, \Delta CCS) = 0.7690 \pm 0.0250$ (95% CI: ± 0.0136), indicating robustness to augmentation randomness within our bounded, non-geometric TTDA regime.

Specifically, we assess robustness along two complementary axes, which are sensitivity to TTDA seeds, and sensitivity to model architectures and training regimes.

a) TTDA configuration and rationale: We use nine non-geometric, mild photometric transforms per image (*mild brightness, mild contrast, mild blur, mild noise, brightness, contrast, noise, sharpen, and color shift*), with parameters sampled from narrow, bounded ranges (e.g., brightness $\alpha \in [0.9, 1.1]$, $\beta \in [-10, 10]$; Gaussian noise $\sigma \in [0.005, 0.01]$; blur kernel $\in \{3, 5\}$). These TTDA follow the “common corruptions” family (noise, blur, weather, digital) used in robust-

ness benchmarks [27], [28] and emulate sensor/illumination variation rather than adversarial effects. They are also standard labels (e.g., “car”) preserving augmentations in augmentation surveys [29], [30]. We intentionally avoid geometric transforms (flip/rotate/scale/crop) so that CCS which relies on IoU, measures detector stability under appearance changes rather than systematic box displacement. Because each augmentation parameter is drawn from a *fixed, narrow interval* (e.g., brightness $\alpha \in [0.9, 1.1]$, noise $\sigma \in [0.005, 0.01]$), changing the random seed only changes which value inside that interval is sampled (e.g., $\alpha = 0.93$ vs. 1.07); it does not change the interval itself (i.e., the maximum strength of the augmentation). This is why the estimates remain stable with tight confidence intervals across seeds (Tab. IV).

b) Inference from Tab. III: Tab. III shows that this congruence remains consistent across varying model architectures (e.g., Faster R-CNN, RetinaNet, SSD) and training epochs (e.g., 2 vs. 250 epochs), highlighting the robustness and model-agnostic nature of CCS. This supports its utility for real-world deployment and continuous model evaluation.

G. Platform and Runtime

1) Platform: **GPUs:** 8× NVIDIA A100-SXM4-40GB (driver 580.65.06, CUDA 13.0). **CPUs:** dual-socket AMD EPYC 7742 (2×64 cores, SMT on; 256 hardware threads), 8 NUMA nodes. **OS:** Ubuntu Linux.

2) Detector forward pass runtime (GPU; context only): With $M=9$ test-time augmentations evaluated sequentially on a single A100 per detector, the *steady-state* per-augmentation forward time is typically 26–33 ms. Summed over the 9 augmentations, this yields ≈ 235 –295 ms per image (median ≈ 265 ms). The very first augmentation after model load is sometimes much slower (~ 600 –650 ms) due to one-off GPU initialization and cuDNN autotuning; we treat this as warm-up and exclude it from summary statistics. Each detector is pinned to a dedicated GPU (e.g., Faster R-CNN \rightarrow GPU 0, RetinaNet \rightarrow GPU 1); all 9 augmentations for that detector run on the same GPU.

3) CCS runtime (CPU):

a) Timing scope and results: We report only CCS post-processing time per image, excluding TTDA generation and detector inference (Tab. V). Note that when we replace the augmentation by introducing Gaussian noise similar to what is done in randomized smoothing [15]–[17], the total execution time will be substantially reduced, and the execution can be completely parallelized. Given M augmentations, CCS evaluates all *ordered* pairs (i, j) with $i \neq j$ (exactly $M(M-1)$ pairs; Eq. (4)). For each pair we: (i) build the IoU matrix $\Omega_{ij} \in \mathbb{R}^{N_i \times N_j}$, (ii) threshold to Ω'_{ij} using β (Eq. (1)), (iii) compute row-wise maxima $\text{MaxIoU}_k^{ij} = \max\{\Omega'_{ij}(k, *)\}$, and (iv) sum and divide by κ_i to obtain γ_{ij} (Eq. (3)). The final averaging over $i \neq j$ to produce CCS (Eq. (4)) is of time complexity $\mathcal{O}(M^2)$ and contributes < 0.1 ms per image, so we omit it from the totals. On our CPU (2×EPYC 7742), with $M=9$ (72 ordered pairs; typical $N_i, N_j \leq 5$), per-pair time is 0.03–0.16 ms and total

CCS time is 2.9–11.4 ms per image, aggregated from per-pair CSV logs.

b) Time complexity: For a specific pair (i, j) , forming Ω_{ij} and taking row-wise maxima has a time complexity of $\mathcal{O}(N_i N_j)$; no assignment is solved. The total per-image cost equals

$$\sum_{i \neq 1}^M \sum_{j=1, i \neq j}^M \mathcal{O}(N_i N_j) \leq \mathcal{O}(M(M-1) \max_i N_i \max_j N_j).$$

In our car/truck setting, typically we have $N_i, N_j \leq 5$, so matrices are tiny and often sparse after thresholding. When the number of objects is large, apart from utilizing GPU parallelization capabilities, one can also only consider safety-relevant objects, i.e., objects that are close by and therefore have larger bounding boxes (as far objects do not matter in terms of driving response). Filtering out small and distant objects additionally ensures that the CCS computation can also be implemented on edge AI accelerators.

V. CONCLUSION

We presented CCS, a label-free, deployment-oriented metric that turns test-time augmentation agreement into a per-image proxy for detector reliability. By aggregating IoU overlaps across mild, non-geometric augmentations, CCS supplies continuous monitoring and side-by-side comparison without ground-truth annotations. In controlled studies on Open Images and KITTI, CCS shows $> 90\%$ congruence with F1-Score, pPDQ, and OC-cost, and remains stable across augmentation seeds and heterogeneous architectures. Using an indifference margin τ , we classify small discrepancies as ties, which highlights substantive disagreements and helps identify underperforming cases. Future work will refine augmentation design and τ selection, accelerate computation, and extend validation to broader datasets and operating conditions.

REFERENCES

- [1] M. Abdar, F. Pourpanah, S. Hussain, D. Rezazadegan, L. Liu, M. Ghavamzadeh, P. Fieguth, X. Cao, A. Khosravi, U. R. Acharya *et al.*, “A review of uncertainty quantification in deep learning,” *Information Fusion*, vol. 76, pp. 243–297, 2021.
- [2] D. Hall, F. Dayoub, J. Skinner, H. Zhang, D. Miller, P. Corke, G. Carneiro, A. Angelova, and N. Sünderhauf, “Probabilistic object detection: Definition and evaluation,” in *IEEE Winter Conference on Applications of Computer Vision (WACV)*, 2020, pp. 1031–1040.
- [3] M. T. Le, F. Diehl, T. Brunner, and A. Knoll, “Uncertainty estimation for deep neural object detectors in safety-critical applications,” in *International Conference on Intelligent Transportation Systems (ITSC)*. IEEE, 2018, pp. 3873–3878.
- [4] A. Kuznetsova, H. Rom, N. Alldrin, J. Uijlings, I. Krasin, J. Pont-Tuset, S. Kamali, S. Popov, M. Mallocci, A. Kolesnikov *et al.*, “The Open Images Dataset V4,” *International Journal of Computer Vision (IJCV)*, vol. 128, no. 7, pp. 1956–1981, 2020.
- [5] A. Geiger, P. Lenz, and R. Urtasun, “Are we ready for autonomous driving? the KITTI vision benchmark suite,” in *IEEE/CVF Conference on Computer Vision and Pattern Recognition (CVPR)*, 2012, pp. 3354–3361.
- [6] S. Ren, K. He, R. Girshick, and J. Sun, “Faster R-CNN: Towards real-time object detection with region proposal networks,” in *Advances in Neural Information Processing Systems (NeurIPS)*, vol. 28, 2015.
- [7] T.-Y. Lin, P. Goyal, R. Girshick, K. He, and P. Dollár, “Focal loss for dense object detection,” in *IEEE International Conference on Computer Vision (ICCV)*, 2017, pp. 2980–2988.

- [8] W. Liu, D. Anguelov, D. Erhan, C. Szegedy, S. Reed, C.-Y. Fu, and A. C. Berg, "SSD: Single shot multibox detector," in *European Conference on Computer Vision (ECCV)*. Springer, 2016, pp. 21–37.
- [9] S. Schmidt, Q. Rao, J. Tatsch, and A. Knoll, "Advanced active learning strategies for object detection," in *IEEE Intelligent Vehicles Symposium (IV)*, 2020, pp. 871–876.
- [10] A. Kendall and Y. Gal, "What uncertainties do we need in Bayesian deep learning for computer vision?" in *Advances in Neural Information Processing Systems (NeurIPS)*, vol. 30, 2017.
- [11] G. Wang, W. Li, M. Aertsen, J. Deprest, S. Ourselin, and T. Vercauteren, "Aleatoric uncertainty estimation with test-time augmentation for medical image segmentation with convolutional neural networks," *Neurocomputing*, vol. 338, pp. 34–45, 2019.
- [12] Y. Yang, W. Wang, Z. Chen, J. Dai, and L. Zheng, "Bounding box stability against feature dropout reflects detector generalization across environments," in *International Conference on Learning Representations (ICLR)*, 2024, spotlight Paper.
- [13] H. Yu, J. Deng, W. Li, and L. Duan, "Towards unsupervised model selection for domain adaptive object detection," in *Advances in Neural Information Processing Systems 37 (NeurIPS)*, 2024.
- [14] W. Yu, S. Zhu, T. Yang, C. Chen, and M. Liu, "Consistency-based active learning for object detection," in *IEEE/CVF Conference on Computer Vision and Pattern Recognition Workshops (CVPRW)*, 2022.
- [15] J. M. Cohen, E. Rosenfeld, and J. Z. Kolter, "Certified adversarial robustness via randomized smoothing," in *International Conference on Machine Learning (ICML)*, 2019, pp. 1310–1320.
- [16] M. Fischer, M. Baader, and M. Vechev, "Certified defense to image transformations via randomized smoothing," in *Advances in Neural Information Processing Systems (NeurIPS)*, 2020.
- [17] P.-Y. Chiang, E. B. Gökcesu, S. S. McGuire, J. Z. Kolter, and A. Odena, "Detection certification via randomized smoothing," in *Advances in Neural Information Processing Systems (NeurIPS) Workshop on Safety and Robustness in Decision Making*, 2020.
- [18] S. Gasperini, J. Haug, M.-A. N. Mahani, A. Marcos-Ramiro, N. Navab, B. Busam, and F. Tombari, "CertainNet: Sampling-free uncertainty estimation for object detection," *IEEE Robotics and Automation Letters*, vol. 7, no. 2, pp. 698–705, 2021.
- [19] D. Feng, A. Harakeh, S. L. Waslander, and K. Dietmayer, "A review and comparative study on probabilistic object detection in autonomous driving," *IEEE Transactions on Intelligent Transportation Systems (T-ITS)*, vol. 23, no. 8, pp. 9961–9980, 2022.
- [20] M. R. Nallapareddy, K. Sirohi, P. L. Drews, W. Burgard, C.-H. Cheng, and A. Valada, "EvCenterNet: Uncertainty estimation for object detection using evidential learning," in *IEEE/RSJ International Conference on Intelligent Robots and Systems (IROS)*. IEEE, 2023, pp. 5699–5706.
- [21] M. Shroff, "Know your neural network architecture more by understanding these terms," arXiv preprint arXiv:2301.XXXXX, 2023.
- [22] M. Otani, R. Togashi, Y. Nakashima, E. Rahtu, J. Heikkilä, and S. Satoh, "Optimal correction cost for object detection evaluation," in *IEEE/CVF Conference on Computer Vision and Pattern Recognition (CVPR)*, 2022, pp. 21 107–21 115.
- [23] A. Harakeh and S. L. Waslander, "Estimating regression predictive uncertainty in deep object detectors," in *International Conference on Learning Representations (ICLR)*, 2021.
- [24] D. Miller, L. Nicholson, F. Dayoub, and N. Sünderhauf, "Dropout sampling for robust object detection in open-set conditions," in *IEEE International Conference on Robotics and Automation (ICRA)*, 2018, pp. 1–7.
- [25] I. Krasin, T. Duerig, N. Alldrin, and et al., "Openimages: A public dataset for large-scale multi-label and multi-class image classification and object detection," in *IEEE International Conference on Computer Vision (ICCV) Workshop*, 2017, pp. 1956–1981.
- [26] A. Geiger, P. Lenz, C. Stiller, and R. Urtasun, "Vision meets robotics: The KITTI dataset," *International Journal of Robotics Research (IJRR)*, vol. 32, no. 11, pp. 1231–1237, 2013.
- [27] D. Hendrycks and T. Dietterich, "Benchmarking neural network robustness to common corruptions and perturbations," in *International Conference on Learning Representations (ICLR)*, 2019.
- [28] C. Michaelis, B. Mitzkus, R. Geirhos, E. Rusak, O. Bringmann, A. S. Ecker, M. Bethge, and W. Brendel, "Benchmarking robustness in object detection: Autonomous driving when winter is coming," in *NeurIPS Workshop on Machine Learning for Autonomous Driving (MLAAD)*, 2019.
- [29] C. Shorten and T. M. Khoshgoftaar, "A survey on image data augmentation for deep learning," *Journal of Big Data*, vol. 6, no. 1, pp. 1–48, 2019.
- [30] A. Mumuni and F. Mumuni, "Data augmentation: A comprehensive survey of modern approaches," *Array*, vol. 16, p. 100258, 2022.